Check for updates

Stable and low-photovoltage-loss perovskite solar cells by multifunctional passivation

Guang Yang[1,2,13], Zhiwei Ren[1,13], Kuan Liu ®[1,13], Minchao Qin ®[3], Wanyuan Deng[1,4], Hengkai Zhang[1], Haibing Wang[2], Jiwei Liang[2], Feihong Ye[2], Qiong Liang[1], Hang Yin[5], Yuxuan Chen[6], Yuanlin Zhuang[2], Siqi Li[7,8], Bowei Gao[9], Jianbo Wang ®[2], Tingting Shi[10], Xin Wang[6], Xinhui Lu ®[3], Hongbin Wu ®[4], Jianhui Hou ®[9], Dangyuan Lei ®[7,8], Shu Kong So[5], Yang Yang ®[11 ✉], Guojia Fang ®[2 ✉] and Gang Li ®[1,12 ✉]

Metal halide perovskite solar cells have demonstrated a high power conversion efficiency (PCE), and further enhancement of the PCE requires a reduction of the bandgap-voltage offset (W_{OC}) and the non-radiative recombination photovoltage loss ($\Delta V_{OC,nr}$). Here, we report an effective approach for reducing the photovoltage loss through the simultaneous passivation of internal bulk defects and dimensionally graded two-dimensional perovskite interface defects. Through this dimensionally graded perovskite formation approach, an open-circuit voltage (V_{OC}) of 1.24 V was obtained with a champion PCE of 21.54% in a 1.63 eV perovskite system (maximum $V_{OC} = 1.25$ V, $W_{OC} = 0.38$ V and $\Delta V_{OC,nr} = 0.10$ V); we further decreased the W_{OC} to 0.326 V in a 1.53 eV perovskite system with a V_{OC} of 1.21 V and a PCE of 23.78% (certified 23.09%). This approach is equally effective in achieving a low W_{OC} ($\Delta V_{OC,nr}$) in 1.56 eV and 1.73 eV perovskite solar cell systems, and further leads to the substantially improved operational stability of perovskite solar cells.

Perovskite solar cells (PSCs) based on three-dimensional (3D) perovskite absorbers have achieved rapid progress with PCE values of over 25% due to the outstanding optoelectronic properties of 3D perovskites. Nevertheless, their poor stability, particularly their susceptibility in humid environments, lack of thermal stability and light-soaking degradation, is a major shortcoming that limits their further practical application.

As the bandgap-voltage offset values of PSCs are still higher than that of GaAs cells ($W_{OC} \approx 0.3$ V),[1] reducing the W_{OC} and pushing the open-circuit voltage of PSCs towards the Shockley–Queisser V_{OC} limit (where there is radiative recombination loss only) is of great significance for boosting the PCE, as well as for understanding the fundamental science more deeply[2–6]. Several studies have shown that non-radiative recombination via defects at the interfaces between the perovskite and charge-transport layers is the main source of voltage losses for PSCs[7–9]. Strategies such as surface passivation or the use of processing additives have been explored to minimize non-radiative recombination losses at interfaces and thus improve the open-circuit voltage of devices[10,11]. For example, surfaces and grain boundaries with potassium passivation have been shown to enable the substantial mitigation of non-radiative recombination losses ($\Delta V_{OC,nr}$), pushing the V_{OC} value up to 1.17 V with a low W_{OC} of 0.39 V ($\Delta V_{OC,nr} = 0.11$ V) for a 1.56-eV-bandgap 3D perovskite system. However, there are still substantial non-radiative losses produced from trap states within the perovskite bulk film, which limits the

performance and stability of the perovskite device[12]. In addition, the energy-level alignment at the interface is also a key factor for minimizing the interfacial non-radiative recombination, which requires careful interface design[13]. Thus, a simultaneous interface and bulk trap passivation strategy as well as interface engineering are required to further reach the full thermodynamic potential of the open-circuit voltage.

In this work, we introduced a multifunctional (bulk and interface) 2D perovskite passivation approach and graded interface design to reduce the photovoltage loss of the PSC and enhance the device stability. n-Butylammonium bromide (BABr) was first coated on top of a 3D perovskite film, and through thermal driving we simultaneously achieved a relatively uniform distribution of self-passivated 2D/3D perovskites in the bulk, covered by graded mixed-dimensional, wider-bandgap 2D perovskite layers. We name it the dimensionally graded perovskite formation (DGPF) approach. This multifunctional approach effectively suppresses the non-radiative recombination loss in both the bulk and at the interface of the perovskite. Via this DGPF technique, we demonstrate a hysteresis-free maximum PCE of 21.54% with a high V_{OC} of 1.24 V in a 1.63 eV perovskite system, and the W_{OC} is only 0.39 V, which is equivalent to a non-radiative recombination V_{OC} loss ($\Delta V_{OC,nr}$) of only 0.11 V. In particular, a minimum W_{OC} of 0.38 V and a $\Delta V_{OC,nr}$ of 0.10 V was achieved in a 20.15% PCE device. We further decrease the W_{OC} to as low as 0.326 V in an approximately 1.53 eV perovskite
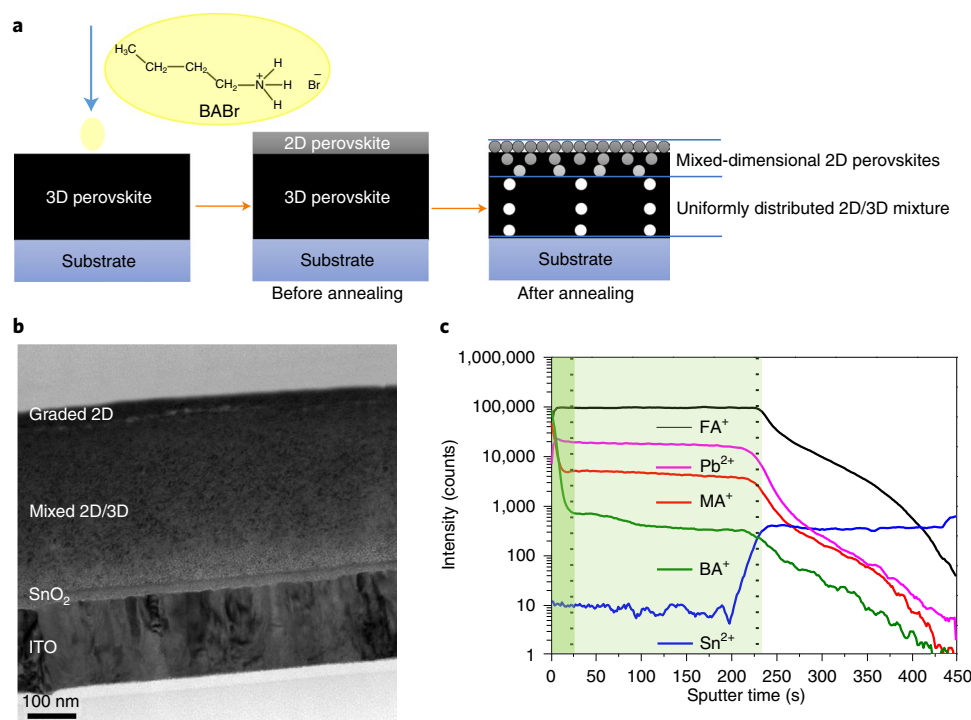
Fig. 1 | Device architecture and ToF-SIMS profiling of DGPF devices. a,b, Schematic diagram (**a**) and cross-sectional TEM image (**b**) of our fabricated DGPF film deposited on the SnO₂-coated ITO substrate. **c**, ToF-SIMS depth profile of the DGPF perovskite film deposited on an ITO substrate. The dark green and light green shaded regions are the surface and bulk of perovskite films, respectively.

system ($\Delta V_{OC,nr} = 74\,mV$), with a maximum V_{OC} of 1.21 V and a champion PCE of 23.78% (a certified PCE of 23.09%). The DGPF approach is also validated by examining hybrid PSCs with band-gaps of 1.56 eV and 1.73 eV, where very low W_{OC} ($\Delta V_{OC,nr}$) and high V_{OC} values were both achieved. At the same time, the 2D perovskite components in the bulk and at the interface provide superb stability under illumination, ensuring that the DGPF device can maintain 91% of its initial efficiency over 500 h of 1-Sun illumination under maximum power point (MPP) conditions.

Design strategy and characterization of DGPF perovskite films

Figure 1a shows the schematic illustration of our DGPF method, and Fig. 1b shows a cross-sectional high-resolution transmission electron microscopy (HRTEM) image of the DGPF perovskite film deposited on the SnO₂-coated indium tin oxide (ITO) substrate, verifying the homogeneity of the 2D perovskite layer on the top of the 3D perovskite film[14]. The RbCsMAFA quadruple-cation 3D perovskite film, where MA is methylammonium and FA is for-mamidinium, was formed using an antisolvent-assisted one-step method[15]; this four-component system has demonstrated a state-of-the-art device performance in several studies reported by researchers at EPFL[15–17]. The quadruple-cation perovskite system has shown not only a high efficiency, but also a higher V_{OC} value (1.16–1.18 V) than a triple-cation (~1.13 V) counterpart (both have a bandgap of around 1.63 eV)[15–17]. The detailed fabrication method of the device is given in the Methods section. Here, to form the mixed 2D/3D perovskite heterojunction films, long-chain BABr molecules were first dissolved in isopropyl alcohol, at different concentrations, and then spin coated directly onto the top of the as-prepared 3D RbCsMAFA perovskite film to form a thin film; this was then followed by thermal annealing at 100 °C for 10 min. This approach leads to the perovskite vertical composition distribution shown below.

To investigate the distribution of ions inside the perovskite films after the introduction of BABr, we conducted time-of-flight secondary-ion mass spectrometry (ToF-SIMS) measurements on the DGPF perovskite films. The ToF-SIMS depth profile shown in Fig. 1c reveals the gradient distribution of BA⁺ with the initial sput-tering time, which indicates that the ultrathin 2D perovskite film was formed on the surface of the 3D perovskite layer. In the bulk (originally pure 3D) perovskite film, we now observe a relatively uniform distribution of BA⁺ with an intensity of over two orders of magnitude lower than that on the surface, indicating a clear diffu-sion process. Therefore, it is evident that the bulk film contains both 3D and 2D perovskite with an increasing 2D concentration towards the surface. Owing to the gradient distribution of BA⁺, the number of layers (n) of the 2D perovskite might increase from the surface to the bulk, creating a tendency for bandgap narrowing (as illustrated in Fig. 1a and Supplementary Fig. 10b).

The grazing-incidence wide-angle X-ray scattering (GIWAXS) technique was used to study the crystal orientation of the control and mixed DGPF perovskite films[18]. The scattering patterns of the perovskite films with various concentrations of BABr are shown in Fig. 2a. The corresponding radial intensity profiles averaged over the whole images are presented in Fig. 2b. The standard pure 3D perovskite film (0-BABr) displays uniform diffraction rings, indi-cating the formation of perovskite polycrystals with a randomly oriented cubic structure. For the perovskite films with the BABr post-treatment, sharp diffraction peaks emerged at scattering vec-tor q values of 0.32, 0.64 and 0.96 Å⁻¹ along the z direction (Fig. 2c), which are indexed as the (020), (040) and (060) planes of layered 2D perovskite crystals parallel to the substrate with a layer spacing, d, of ~20 Å ($n = 2$)[19]. The parallel 2D perovskite orientation is surprising as it is commonly considered to be unfavoured for overall vertical charge transport in solar-cell devices. However, the high-efficiency PSC in this study indicates that the 2D perovskite layer with a rela-tively larger bandgap is thin enough for carrier transport and can

act as an effective electron-blocking layer to suppress the interfacial charge recombination. The BABr GIWAXS peak appearing at $q_z = 0.41\,\text{Å}^{-1}$ in the pure BABr film (Supplementary Fig. 1a) and the excess PbI_2 peak appearing at $q_z = 0.92\,\text{Å}^{-1}$ in the 3D perovskite film were both absent, suggesting that 2D perovskite layers are partially formed from the reaction of BABr with excess PbI_2. When the concentration of BABr is increased, the 2D perovskite peaks become more intense, as the higher order (080) peak appears with the $5\,\text{mg ml}^{-1}$ BABr treatment.

To provide more detailed evidence of the graded 2D perovskite from the surface to the bulk, we conducted GIWAXS analysis at different X-ray incident angles to elucidate the vertical structure of the surface and internal perovskite layers with depth-dependent characterization, as shown in Supplementary Fig. 2. The structure information of the perovskite film surface was recorded at a small incident angle of 0.1°, which shows the formation of a 2D perovskite layer with $n = 2$ only. When the angle of incidence was increased to 0.3°, we clearly observed some additional diffraction peaks, which are assigned to be the (0k0) plane of the 2D perovskite with $n = 3$. With increasing the incident angle and penetration depth, the diffraction peak intensity of the 2D perovskite with $n = 2$ and 3 gradually increased. We can also clearly distinguish the (222) plane of the 2D perovskite with $n = 2$, 3 and 4 at an incident angle of 1°. Thus, the depth-dependent GIWAXS results are in good agreement with our hypothesis of graded top 2D perovskite layers with increasing n values for top-down distribution. To further evaluate the structural properties of the DGPF perovskite films, we performed HRTEM measurements using the focused ion beam (FIB) lift-out technique shown in Supplementary Fig. 3, which allows the crystal structure to be probed throughout the perovskite film. Here, we selected two regions (1 and 2), which correspond to the top surface and the bulk, respectively. Region 1 (the top surface) shows lattice fringes with a characteristic d spacing of 13 Å, which can be ascribed to 2D perovskite phases with $n = 1$. In Region 2 (the bulk film), we can observe the characteristic d spacing of the 3D perovskite phase (3.2 Å). Besides, it is worth noting that the 2D perovskite phases with $n = 2$ and 3 were embedded within the 3D perovskite phases, which are probably located at the grain boundary.

The influence of the annealing time on the perovskite film was also investigated, as shown in Supplementary Fig. 1. The 2D perovskite signals remain almost the same for the samples with and without annealing, whereas the 3D perovskite signals become stronger with a longer annealing time. The diffraction peaks shift towards larger q values, indicating a slight lattice contraction[20]. This is attributed to substitution of the larger I^- ions with the smaller Br^- ions in the 3D perovskite crystals. The longer the annealing time, the more BABr diffuses into the bulk film, causing a larger lattice contraction, which is consistent with the ToF-SIMS results. Therefore, as illustrated in Fig. 2d, upon BABr post-treatment, BA^+ and Br^- ions tend to fill the vacancies at the grain boundaries of the 3D perovskite due to the strong reactivity of the introduced BA^+ and Br^- ions with existing dangling bonds[21]. In this case, the 2D perovskite phases are most likely to form at the grain boundaries surrounding the 3D perovskite phases. The 2D perovskite will heal and passivate the 3D perovskite defects, notably reducing the non-radiative recombination, which is in agreement with the observed lower V_{OC} loss presented in the following text.

The perovskite film morphology is another critical factor for the photovoltaic performance. Top-view scanning electron microscopy (SEM) images and atomic force microscopy (AFM) images of the control and DGPF perovskite films are shown in Fig. 2e. The morphology of the control RbCsMAFA perovskite film is uniform and compact with well-crystallized grains, which is in good agreement with a previous study[15]. With BABr treatment, an obvious grain-coarsening process is observed, that is, the original small perovskite grains were merged into larger ones via a thermodynamically spontaneous Ostwald ripening process[22]. We expected that the BABr molecules would gradually penetrate into the existing 3D perovskite crystalline structure, resulting in the formation of thin 2D perovskite phases on the top and in the bulk of the mixed 2D/3D perovskites film. When a low concentration of BABr solution is used (1 or $2\,\text{mg ml}^{-1}$), we observe both large and small grains. It is reasonable to expect that in the low-concentration cases, the amount of BABr is not sufficient for recrystallizing all of the small-grain-sized 3D perovskite crystals. With a further increase in the BABr concentration to $5\,\text{mg ml}^{-1}$, the surface morphology becomes smoother with uniformly distributed grain sizes.

Device performance and characterization

Photovoltaic devices were fabricated using spiro-OMeTAD as a hole-selective layer and gold as the counter electrode. The current density–voltage (J–V) curves of the champion control and DGPF PSCs are shown in Fig. 3a. The control RbCsMAFA-based planar PSC device shows a decent champion PCE of 19.61% with a short-circuit current density (J_{SC}) of $22.25\,\text{mA cm}^{-2}$, a V_{OC} of 1.161 V and a fill factor (FF) of 75.92%. Compared with the data on mesoporous PSCs reported by the researchers at EPFL, the V_{OC} and J_{SC} values are very similar, whereas the FF is lower (0.76 versus 0.81). After BABr treatment, the DGPF PSC shows a clear performance enhancement, yielding a champion PCE of 20.24% when using $1\,\text{mg ml}^{-1}$ BABr and 21.54% when using $2\,\text{mg ml}^{-1}$ BABr, with an impressive V_{OC} of 1.24 V (Fig. 3a and Supplementary Fig. 4). We fabricated 20 individual devices for both control and DGPF PSCs at $2\,\text{mg ml}^{-1}$ BABr. The statistics of two types of devices are shown in Supplementary Fig. 5, which indicates good reproducibility in the DGPF PSCs with an improved PCE of 20.38% ($\pm0.38\%$) on average compared with 18.80% ($\pm0.31\%$) in the control PSCs. There is a much enhanced average V_{OC} of 1.22 V (±0.02 V) in the DGPF PSCs, compared with 1.15 V (±0.02 V) in the pure 3D PSCs, and this is the major factor contributing to the overall efficiency enhancement. Considering the very similar optical bandgap values for the control and DGPF perovskite films, the driving force of the high V_{OC} value with a small W_{OC} for the DGPF PSCs is of great interest.

The external quantum efficiency (EQE) data of the PSCs with different BABr concentrations are shown in Supplementary Fig. 4b. As expected, the EQE spectrum is slightly blue shifted when BABr is incorporated, although this is very small and does not lead to a reduction of the J_{SC}. We observed a better photoresponse in the long-wavelength range for the devices treated with BABr solutions, which may originate from enhanced charge transport[23]. For the RbCsMAFA system, when using an optimized BABr solution concentration of $2\,\text{mg ml}^{-1}$, the cell is hysteresis-free (as shown in Fig. 3a) with a PCE of 21.54%, and the stabilized PCE is 21.27% (as shown in Supplementary Fig. 6). Here, we also compared the results of some PSCs with a PCE of over 21%, where

Fig. 2 | Crystallinity and morphology of the perovskite films. a, 2D GIWAXS patterns of the control (0 mg ml⁻¹ BABr) and DGPF perovskite films with BABr solutions of various concentrations (1, 2 and 5 mg ml⁻¹). **b**, Radial intensity profiles averaged over the entire 2D GIWAXS image. **c**, Intensity profiles along the q_z axis. **d**, Schematic of 2D/3D perovskite film formed via the DGPF method. A thin 2D perovskite capping layer with mixed-dimensionality is formed on top of the 3D perovskite film, and the 2D perovskite phase can be further produced between the grain boundaries of the 3D counterparts leading to the formation of the mixed 2D/3D perovskite. **e**, Top-view SEM (upper) and surface AFM (lower) images of the control and DGPF perovskite films with different BABr concentrations.

the W_{OC} varies from 0.39 to 0.48 V, and where our DGPF device compares favourably amongst them (Supplementary Fig. 7 and Supplementary Table 3)[15,24].

Elucidating DGPF PSC V_{OC} loss mechanisms

To understand the reason of the high V_{OC} in these PSCs in a quantitative manner, the accurate determination of the perovskite band-
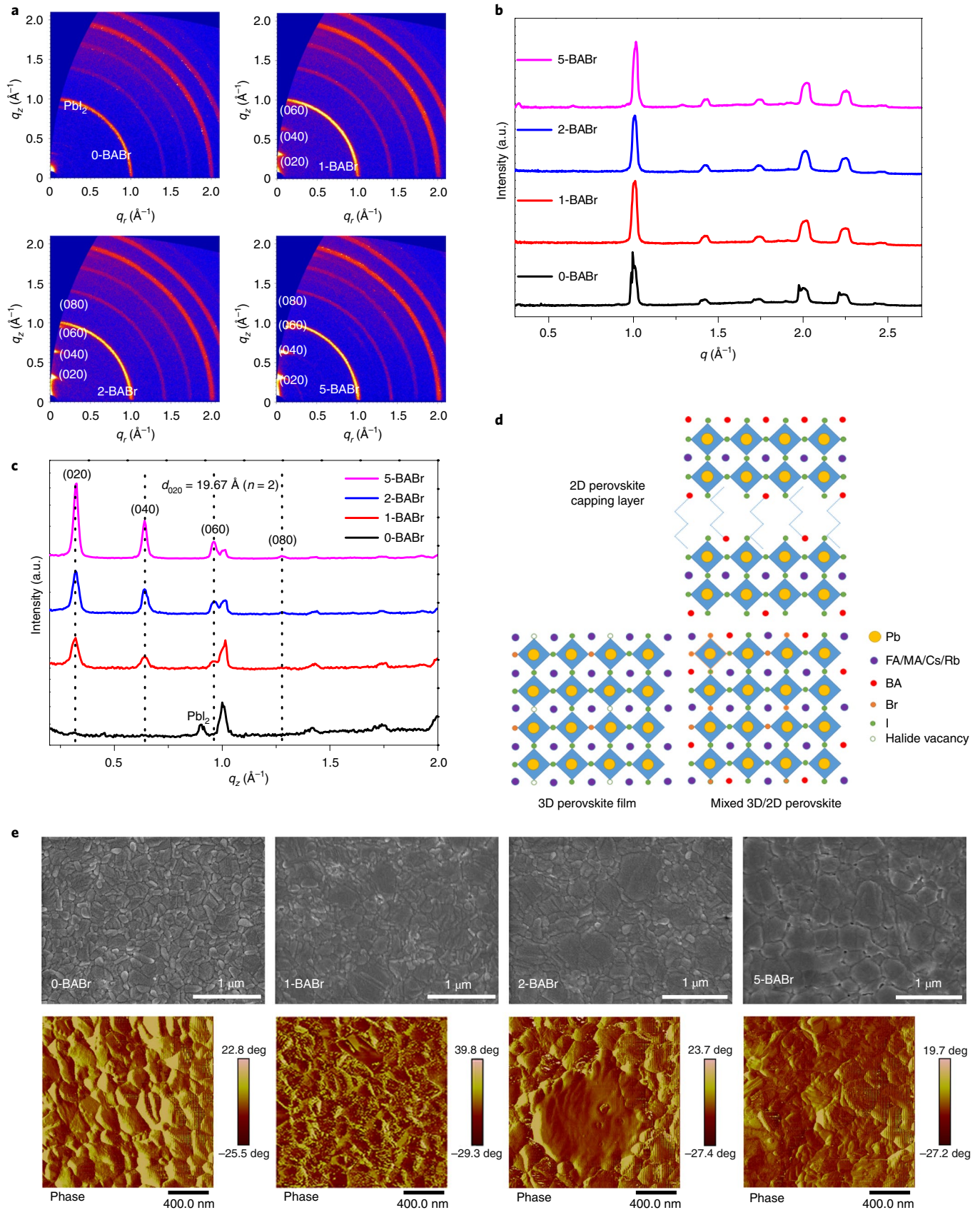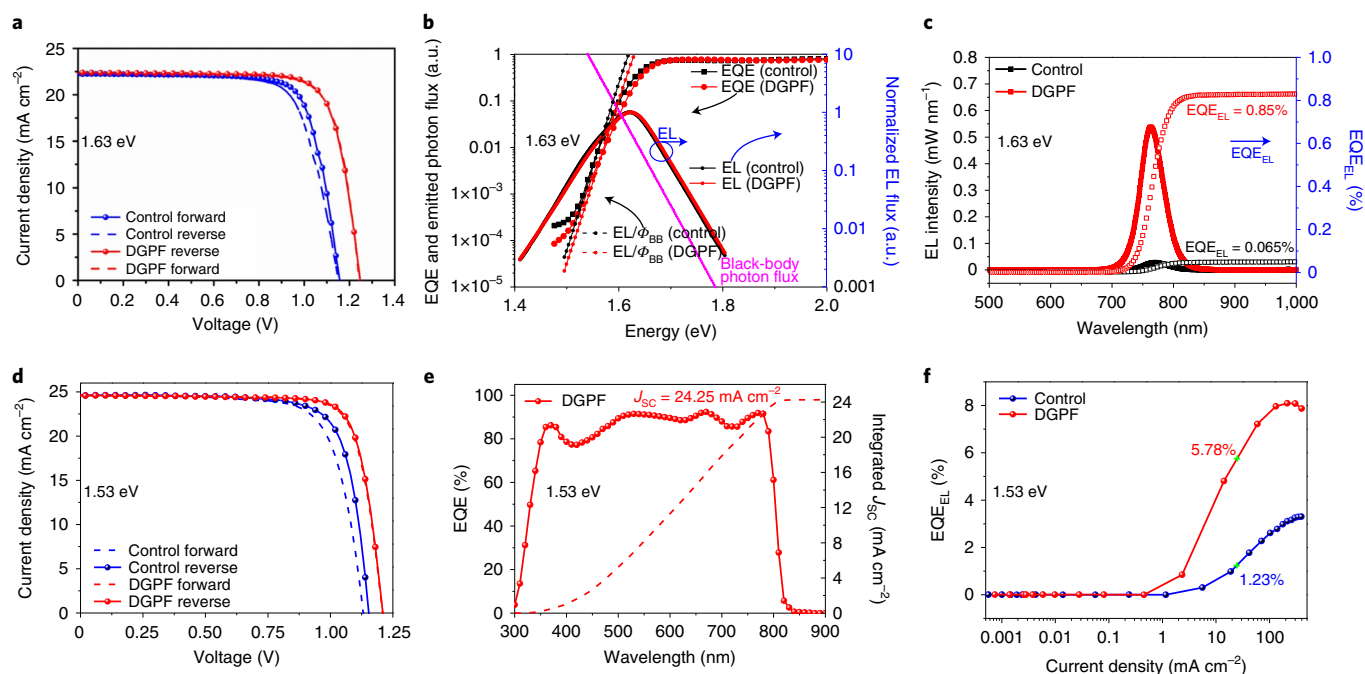
Fig. 3 | Photovoltaic performance and optoelectronic properties of the PSCs. a, J–V curves obtained from forward and reverse scan directions for the champion control and DGPF devices based on the 1.63 eV perovskite composition. **b**, EQE and electroluminescence (EL) spectra for the control and DGPF-based perovskite devices. **c**, Calculated EQE$_{EL}$ quantum efficiency (open symbols) derived from the EL spectrum at an injection current density of 22 mA/cm^2. Here, the measured V_{OC} values for the control (0-BABr) and DGPF (2-BABr) PSCs are 1.16 V and 1.23 V, respectively. **d**, J–V curves of the champion control and DGPF-based devices in a ~1.53 eV perovskite system from forward and reverse scan directions. **e**, EQE spectrum of the DGPF-based device with an integrated J_{SC} of 24.25 mA cm^{-2}. **f**, EQE$_{EL}$ as a function of the injection current density for the control and DGPF-based PSCs when operating as LEDs.

gap is critical. As shown in Supplementary Fig. 8, the determination of optical bandgap (E_g) values was conducted using two widely recognized methods: (1) using the maximum point of the derivative of the EQE spectrum (that is dEQE/dE)[25] and (2) using the Tauc plot[26]. The E_g values from the two methods agree very well.

We first examine the electroluminescence (EL) efficiency. The reciprocity relation can describe the relationship between the photovoltaic quantum efficiency (EQE$_{PV}$) and the external quantum efficiency of the electroluminescence (EQE$_{EL}$), which can be used to quantify the V_{OC} loss in photovoltaic devices[27]. According to Rau, $\Phi_{EL}(E) = \varphi_{BB}(E)\,EQE_{PV}(E)\left[\exp\left(\frac{qV}{kT}\right) - 1\right]$, where $\varphi_{BB}(E)$ is the black-body emission flux density, $\Phi_{EL}(E)$ is the EL spectral photon flux ($\Phi_{EL}(E) = \frac{J_{inj}(V)}{q}\,EQE_{EL}(E)$), $J_{inj}(V)$ is the injected current, V is the applied internal voltage, k is the the Boltzmann constant, T is the temperature, and q is the elementary charge. As shown in Fig. 3b, the extracted EQE$_{PV}$ exhibited a nearly exact dependence on the energy as the measured EQE$_{PV}$, implying that the reciprocity relation holds. Herein, we identify the origins of the increased open-circuit voltage in the DGPF PSCs by quantifying the dominating recombination mechanisms. The $V_{OC,rad}$ describes the radiative limit of V_{OC}, which is determined by $V_{OC,rad} = \frac{kT}{q}\ln\left[\frac{J_{SC}}{\int_0^\infty EQE_{PV}(E)\varphi_{BB}(E)\mathrm{d}E} + 1\right]$ (ref. [6]). The calculated $V_{OC,rad}$ value is 1.35 V for both the reference control and DGPF perovskite devices, both with almost the same 1.63 eV bandgap[28]. Therefore, the difference in the non-radiative recombination losses is the source of the V_{OC} enhancement. We then quantify the non-radiative recombination voltage loss ($\Delta V_{OC,nr}$), which in principle can be estimated from the measured EQE$_{EL}$ using the relationship $\Delta V_{OC,nr} = V_{OC,rad} - V_{OC} = -\frac{kT}{q}\ln EQE_{EL}$. An EQE$_{EL}$ value of 0.85% was measured for a DGPF PSC device under

light-emitting diode (LED) mode with a forward-bias current density of 22.22 mA cm^{-2} (Fig. 3c). This EQE$_{EL}$ value is very close that of the most efficient silicon solar cell (~0.5%)[29]. This is also one of the highest values obtained in PSCs. The 0.85% EQE$_{EL}$ corresponds to a $\Delta V_{OC,nr}$ value of 0.12 V (refs. [15,30]), which agrees well with the device parameter ($V_{OC} = 1.23$ V for the tested device). For the champion efficiency device with a V_{OC} of 1.24 V, the EQE$_{EL}$ value should be higher and the $\Delta V_{OC,nr}$ will be 0.11 V. The maximum V_{OC} of 1.25 V with the 20.15% PCE for the DGPF PSC device indicates a $\Delta V_{OC,nr}$ value of 100 mV (Supplementary Fig. 9). On the other hand, the control PSC has a V_{OC} of 1.16 V. Under the forward-bias LED mode with the same injected current density of 22.22 mA cm^{-2}, the PSC delivers an EQE$_{EL}$ of 0.065% (corresponding to a $\Delta V_{OC,nr}$ value of 0.19 V from the equation), which also agrees well with the device V_{OC} loss analysis. The extraordinarily low non-radiative recombination losses in DGPF PSCs are the dominating reason behind the high V_{OC} as well as the high efficiencies in these PSC devices. Generally, these non-radiative recombination losses arise from defects (charge-carrier traps) either in the bulk photovoltaic materials or at the interfaces.

Ultraviolet photoelectron spectroscopy (UPS) on the 3D perovskite films with different BABr concentrations was carried out to understand the electronic properties of the films. Supplementary Fig. 10a shows the cutoff energy (E_{cutoff}) in the high-binding-energy region and the valence band with respect to the vacuum level derived from the UPS spectra. With the increase in BABr concentration, the E_{cutoff} shifts to a higher binding energy, indicating that the ion-exchange-induced 3D to 2D phase transition can reduce the Fermi level of RbCsMAFA[19]. The valence-band edges determined from the linear portion in the low-binding-energy region for 0-BABr, 1-BABr, 2-BABr and 5-BABr are located at 5.86, 5.80, 5.74 and 5.70 eV, respectively. Here, to mimic a similar situation, thinner 3D perovskite films (at around 100 nm) with and without

Table 1 | Photovoltaic parameters and voltage-loss analysis of the best-performing PSCs

Perovskite composition	Condition	E_g^a (eV)	V_{OC} (V)	J_{SC} (mA cm^{-2})	FF (%)	PCE (%)	$\Delta V_{OC,SQ}^b$ ($\Delta V_{OC,rad}^c$) (V)	$\Delta V_{OC,nr}^d$ (V)
MA$_{0.7}$FA$_{0.3}$PbI$_3$	Control	1.555	1.094	22.68	74.77	18.58	0.273	0.188
	DGPF	1.561	1.160	22.95	77.57	20.67	0.273	0.128
RbCsMAFA (I:Br = 0.83:0.17)	Control	1.628	1.161	22.25	75.92	19.61	0.283	0.184
	DGPF	1.632	1.240	22.37	77.65	21.54	0.283	0.109
FA$_{0.8}$Cs$_{0.2}$Pb(I$_{0.7}$Br$_{0.3}$)$_3$	Control	1.733	1.212	18.24	73.21	16.18	0.285	0.236
	DGPF	1.737	1.260	18.44	77.82	18.08	0.285	0.192
Cs$_{0.03}$(FA$_{0.97}$MA$_{0.03}$)$_{0.97}$Pb(I$_{0.97}$Br$_{0.03}$)$_3$	Control	1.533	1.154	24.60	76.50	21.71	0.272	0.107
	DGPF	1.536	1.210	24.57	80.00	23.78	0.272	0.054

^{a}E_g was derived from the average value of E_g^{EQE} and E_g^{Tauc}.IP, inflection point. ^{b}$\Delta V_{OC,SQ}$ (the recombination photovoltage loss at the Shockley–Queisser limit) was calculated, as a function of the bandgap, using the detailed balance principle. ^{c}$\Delta V_{OC,rad} = E_g/q - V_{OC,rad}$, and this is only available for the 1.63 eV perovskites shown in this table. ^{d}$\Delta V_{OC,nr}$ was calculated from W_{OC} and $\Delta V_{OC,SQ}$ or $\Delta V_{OC,rad}$.

BABr treatment are used to enhance the signal-to-noise ratio. The absorption spectra of the thin control and DGPF perovskite films are shown in Supplementary Fig. 11. It is noteworthy that the absorption peaks can be observed at 2.27, 2.05 and 1.81 eV, which are assigned to 2D perovskites with $n = 2$, 3 and 4, respectively. As discussed above, the depth-dependent GIWAXS data also confirmed this graded distribution. The top-down structure information shows that the 2D perovskites with a small n value ($n = 2$) are prone exist near the surface. Owing to the graded distribution of BA$^+$ in the 2D perovskite region (Fig. 1c), the energy diagram at the perovskite/hole-transport layer interface can be estimated[31]. As shown in Supplementary Fig. 10b, the energy diagram of a perovskite with a gradient energy structure distribution for the 2 mg ml^{-1} BABr-treated case is depicted. Compared with the pure 3D perovskite device, the graded 2D perovskites lead to a graded energy-level transition from the bulk 3D perovskite to the 2D perovskite. The energy-level shift is not linear, as envisioned from the BA$^+$ spatial distribution. We can expect that the energy-level gradient is smooth close to bulk perovskite, but the gradient is much faster when reaching the spiro-OMeTAD hole-transport layer side. Therefore, the aforementioned graded 2D perovskite layer can be regarded as having the same function as the graded window layer in traditional thin-film solar cells, which provides a potential barrier for the electrons[32]. The electrons moving towards the perovskite top surface (where the trap-state density is higher than that in the bulk) will be reflected back close to the interface. Hence, this energy-level alignment will further eliminate the surface recombination effectively. In the meantime, the mildly graded valence-band energy-level-alignment transition can also facilitate efficient hole transport from the perovskite to the hole-transport-layer material.

Photoluminescence (PL) and time-resolved PL measurements were conducted for the various perovskite films to examine the defect-passivation effect (Supplementary Fig. 12). For the DGPF perovskite films, in addition to a notable PL intensity enhancement, we observed a slight blue shift of the PL peaks, which agree with the scenario of the substitution of I$^-$ with Br$^-$ and the resulting shrinkage of the 3D crystal lattice. The carrier lifetime of the control perovskite film was substantially increased in the self-passivated DGPF perovskite films. All DGPF perovskite films exhibit a long exponential PL decay tail with PL lifetimes of above 1 μs (in particular, a PL lifetime of 1.86 μs was obtained for the 2-BABr sample), in contrast with the shorter lifetime (0.76 μs) for the control perovskite film. This is consistent with the higher voltages shown in Fig. 3c for the DGPF perovskite device in which the defects were effectively passivated[33]. Furthermore, we measure the external PL quantum efficiency (PLQE) for the perovskite films with different contacts. The geometry of the PL measurements is shown in Supplementary Fig. 13, in which the light excitation is

either from top- or bottom-side. Here we used an incident laser with a wavelength of 485 nm, which has a penetration depth of less than 100 nm according to Snell's law, and which implies that we can mainly collect the PL signal near the top surface of the perovskite film under the front excitation[34]. The PLQE of the DGPF perovskite film deposited on the glass reaches a value of 13.58%, whereas it is only 4.65% for the control perovskite film. In the presence of charge-selective contacts (electrons or holes), the PLQE values for both the control and DGPF perovskite films decrease, which can be ascribed to the quenching effect and the introduction of non-radiative channels at the contact interface[35]. We again observe that the DGPF approach enables a less notable reduction in PLQE in the presence of selective contacts. In the case of light excitation from either the top or the bottom, the higher PLQEs for the DGPF perovskite samples suggest that the optoelectronic properties of the perovskite film as well as its related interfaces and surfaces can be optimized via the DGPF method.

The highly sensitive photothermal deflection spectroscopy (PDS) technique was used to study the sub-bandgap/trap-state absorption and energetic disorder in these samples[36]. A decrease in sub-bandgap absorption determined using PDS is clearly seen in the DGPF perovskite films, indicating reduced sub-bandgap states (trap states). The presence of electronic sub-bandgap trap states is one of the origins of non-radiative recombination pathways[37,38]. The internal passivation derived from participation of the 2D perovskite in the final DGPF perovskite film can effectively suppress non-radiative recombination to incur minimal voltage losses. The PDS results come with a characteristic Urbach energy. The Urbach energy values, estimated from the PDS spectra, are 20.55, 19.7, 19.9 and 23.21 meV for samples treated with BABr concentrations of 0, 1, 2 and 5 mg ml^{-1}, respectively (Supplementary Fig. 14). The lower Urbach energy indicates a lower level of electronic disorder in the perovskite films with a low concentration of BABr treatment, which agrees with the enhancement of V_{OC} (ref. [39]). When increasing the BABr concentration to 5 mg ml^{-1}, we observe a slight band-edge absorption rise, indicating increased energy disorder. As the inherent Urbach energy in a 2D perovskite is higher compared with its 3D counterpart, this is expected and is also consistent with the decreasing device performance when treating with a higher BABr concentration. The PDS results for a 2D perovskite are shown in Supplementary Fig. 15, which shows that the Urbach energy of the 2D perovskite is 38.4 meV.

Generality of DGPF strategy in PSCs

We further performed electronic structure calculations based on density functional theory (DFT) to investigate the passivation mechanism at the BA/perovskite interface. The surface terminated with the (110) plane was used for the calculations. Charge-density

calculations based on DFT were performed to characterize how an amine, including the BA molecule, can passivate the $Cs_{0.125}FA_{0.875}Pb(I_{0.85}Br_{0.15})_3$ surfaces. Modelling shows that antisite defects such as Pb_{Br} or Pb_I, known as deep-level defects, are the most detrimental defects in PSCs[40]. As illustrated in Supplementary Fig. 16, the charge distribution is localized around the antisite defect site, which can produce the recombination centre and capture the carriers. After interaction with the BA moiety, we first find that the nitrogen will bond with lead atoms and then the previous antisite defect can be passivated, as shown in Supplementary Fig. 16c, like the perfect surface without any defects indicated by Supplementary Fig. 16b. Without the BA dopant, the localized electron distribution is observed clearly in Supplementary Fig. 16a. The adsorption of BA will make the charge distribution delocalized, indicating that the trap states caused by antisite defects are passivated. The trap density of states of the control and DGPF devices is further examined and shows a much lower trap density of states in the DGPF devices, which is consistent with the DFT calculations (Supplementary Fig. 17).

The effectiveness of the DGPF approach has been validated in more perovskite systems. In the double-cation $MA_{0.7}FA_{0.3}PbI_3$ perovskite system, X-ray diffraction measurements were conducted to analyse the crystal structure of the formed DGPF perovskite film (Supplementary Fig. 18). The perovskite film shows a slight peak shift towards higher 2θ values, which is consistent with findings from the quadruple-cation RbCsMAFA perovskite system. The GIWAXS results in Supplementary Fig. 19 clearly show the 2D diffractive peaks for the BABr-treated samples. The formed 2D perovskite top layer consists of layered 2D perovskites with different n values ($n = 2$ and 3). The device performance based on this narrower-bandgap perovskite ($MA_{0.7}FA_{0.3}PbI_3$, $E_g = 1.55$ eV) is shown in Supplementary Fig. 20. The best-performing $MA_{0.7}FA_{0.3}PbI_3$ PSC with post-treatment of BABr ($E_g = 1.56$ eV) at 2 mg ml^{-1} exhibits a V_{OC} value of 1.161 V, a J_{SC} of 22.95 mA cm^{-2} and a FF of 77.67%, featuring a high PCE of 20.67%. For comparison, the control pure 3D device has a lower PCE of 18.59%. The significantly enhanced V_{OC} for the DGPF PSCs is associated with a clearly reduced V_{OC} deficit, that is, a W_{OC} value of 0.40 V.

This method was also tested in wide-bandgap mixed-cation lead PSCs, which have the significance of being potentially ideal wide-bandgap subcells for tandem perovskite PSCs towards higher efficiency[41,42]. By means of the DGPF approach, the best-performing wide-bandgap $FA_{0.8}Cs_{0.2}Pb(I_{0.7}Br_{0.3})_3$ PSC ($E_g = 1.73$ eV) has a PCE of 18.09% with a W_{OC} value of 0.48 V and an outstanding V_{OC} of 1.26 V (Supplementary Fig. 21)[43]. This again shows one of the highest V_{OC} and lowest W_{OC} values in ~1.73 eV bandgap PSCs, to our knowledge[44]. Hysteresis analysis of representative PSCs based on various optical bandgaps is shown in Supplementary Fig. 22 and summarized in Supplementary Table 4. After the incorporation of BABr, devices shows lower J–V hysteresis compared with the control pure 3D PSC device, which is consistent with the scenario that larger BA moieties mitigate or even prohibit ion migration and reduce the above-mentioned defects. The data of voltage-loss analysis in perovskite devices with different bandgaps are summarized in Table 1.

We further proved the effectiveness of the DGPF approach in a ~1.53 eV perovskite system ($Cs_{0.03}(FA_{0.97}MA_{0.03})_{0.97}Pb(I_{0.97}Br_{0.03})_3$) with a modified SnO_2 quantum dot (QD) electron-transport layer (ETL). A champion PCE of up to 23.78% (average PCE: 23.24 ± 0.33%, certified PCE: 23.09%; Supplementary Fig. 27) with a maximum V_{OC} of 1.210 V (and a W_{OC} value as low as 0.326 V) was achieved, as shown in Fig. 3d. The bandgap of the perovskite was calculated through the combination of EQE and UV-visible absorption spectra (see Supplementary Figs. 23 and 24). More details can be found in Supplementary Figs. 25–27 and Supplementary Table 7. To evaluate the $\Delta V_{OC,nr}$, we measured the EQE_{EL} for a complete PSC device operating as an LED in forward-voltage bias, as shown in Fig. 3f. The DGPF device exhibited an EQE_{EL} of up to 5.78% at an
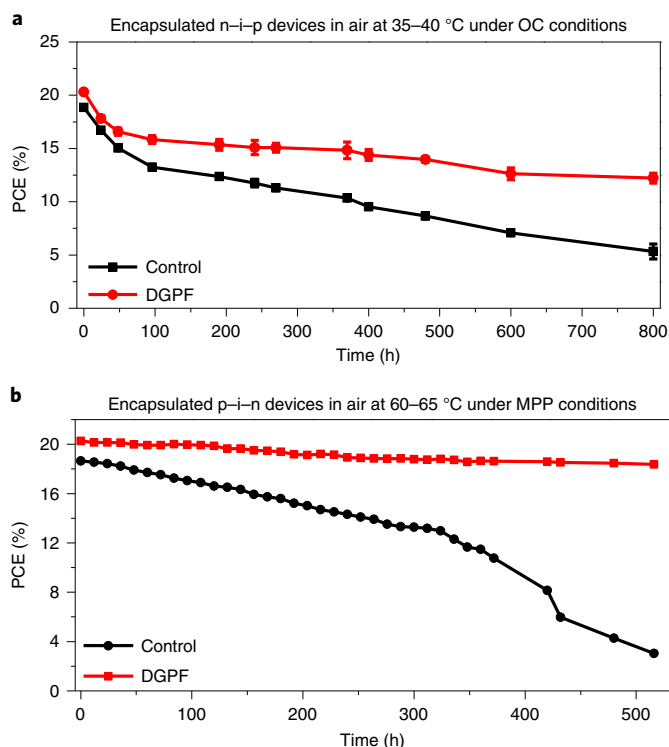

Fig. 4 | Operational stability of the control and DGPF devices. Device-stability parameters of the control and DGPF perovskite devices with encapsulation. Data were obtained from current density–voltage scans over time for the devices. **a**, The n–i–p devices are kept under a white LED array of 0.8-Sun intensity under OC conditions (20–30% RH, 35–40 °C). **b**, The stability data were determined from MPP tracking of p–i–n devices illuminated using 1-Sun irradiation of an LED lamp under ambient conditions (30–40% RH, 60–65 °C).

injection current equal to a J_{SC} of 24.57 mA cm^{-2}, corresponding to a $\Delta V_{OC,nr}$ of 74 mV, which agreed well with the estimated value from the W_{OC}. To the best of our knowledge, the W_{OC} value of 0.326 V is amongst the lowest in all reported perovskite systems.

Device stability

In addition to the device performance, the operational stability of the PSCs is vital for PSC technology. We first investigated the long-term stability of the control and DGPF PSCs (non-encapsulated) under dark storage in ambient conditions with 30% relative humidity (RH; Supplementary Fig. 28). The DGPF PSCs showed a substantially enhanced resistivity to humidity, with virtually no PCE degradation after 45 days. This is attributed to the improved hydrophobicity of the perovskite structure after introduction of the large organic cation (BA). We further studied the stability of the encapsulated devices under continuous simulated sunlight illumination (~35 °C) at open-circuit (OC) conditions. The DGPF PSCs showed a much slower performance degradation compared with the pure 3D PSCs. The encapsulated DGPF PSCs retained 62% of their initial PCE after 800 h of illumination, whereas the control 3D PSCs retained only 25% of their original PCE under the same conditions (Fig. 4). All the device parameters recorded during the stability test (Supplementary Fig. 29a,b) are shown in Supplementary Tables 5 and 6. A 'burn-in' exponential degradation regime was clearly observed in both types of device, which is a common phenomenon for PSCs and organic solar cells[25,45,46]. More specifically, both types of PSC experienced a faster performance degradation process (up to around 100 h), followed by a slower steady degradation. For the encapsulated DGPF

PSCs, the post-burn-in lifetime T_{80} value (that is, the time taken to lose 20% of the initial PCE) is 700 h under 0.8-Sun illumination. However, the T_{80} post-burn-in lifetimes for the pure 3D PSC devices are much shorter, at around 300 h. To exclude the effects of interface layers (particularly the spiro-OMeTAD hole-transport-layer material) and the electric load (under MPP or OC conditions) on the operational stability of the device, we fabricated perovskite devices with a planar p–i–n structure (Supplementary Fig. 30a,b) and tested the long-term stability of encapsulated devices illuminated under continuous 1-Sun irradiation using an LED lamp at a temperature of ~60 °C in air, as shown in Fig. 4b[45]. Under MPP conditions, we found that both the control and DGPF devices showed clearly decreased degradation rates compared with those under OC conditions, which can be ascribed to the role of the excess charge carrier[47,48]. In concusion, our DGPF devices can retain 91% of their initial efficiency after 516 h of operation under continuous illumination in ambient air. In comparison, the control device retained only 16% of the original PCE under the same conditions.

In summary, we developed a simple DGPF self-passivation strategy for high-performance PSCs, which achieved the simultaneous passivation of both bulk and interface 2D perovskites of the PSCs. The DGPF strategy dramatically boosts the PCE of 1.63 eV quadruple-cation PSCs to 21.54%, with a superb V_{OC} of 1.24 V; we further improved the PCE to 23.78% (certified 23.09%) with the maximum V_{OC} of 1.21 V in a ~1.53 eV perovskite system, that is, a W_{OC} value as low as 0.326 V. Non-radiative recombination losses in the perovskite materials and devices can be reduced to as low as 74 mV (from EQE_{EL} measurements), which is one of the lowest reported so far. The method is universally applicable to PSCs of different bandgaps. Moreover, substantially enhanced operational stability is achieved via the simultaneous passivation of 2D perovskites in the bulk and at the interfaces. The DGPF approach paves the way to further approach the theoretical PSC efficiency limit via the elimination of non-radiative recombination decay, and is a step forward in achieving highly efficient PSCs with long-term operational stability.

Online content

Any methods, additional references, Nature Research reporting summaries, source data, extended data, supplementary information, acknowledgements, peer review information; details of author contributions and competing interests; and statements of data and code availability are available at https://doi.org/10.1038/s41566-021-00829-4.

References

1. Jeon, N. J. et al. A fluorene-terminated hole-transporting material for highly efficient and stable perovskite solar cells. *Nat. Energy* **3**, 682–689 (2018).
2. Green, M. et al. Solar cell efficiency tables (version 57). *Prog. Photovolt. Res. Appl.* **29**, 3–15 (2020).
3. Hardin, B. E., Snaith, H. J. & McGehee, M. D. The renaissance of dye-sensitized solar cells. *Nat. Photonics* **6**, 162–169 (2012).
4. Tress, W. et al. Predicting the open-circuit voltage of CH₃NH₃PbI₃ perovskite solar cells using electroluminescence and photovoltaic quantum efficiency spectra: the role of radiative and non-radiative recombination. *Adv. Energy Mater.* **5**, 1400812 (2015).
5. Yin, W.-J., Yang, J.-H., Kang, J., Yan, Y. & Wei, S.-H. Halide perovskite materials for solar cells: a theoretical review. *J. Mater. Chem. A* **3**, 8926–8942 (2015).
6. Yao, J. et al. Quantifying losses in open-circuit voltage in solution-processable solar cells. *Phys. Rev. Appl.* **4**, 014020 (2015).
7. Luo, D. et al. Enhanced photovoltage for inverted planar heterojunction perovskite solar cells. *Science* **360**, 1442–1446 (2018).
8. Zheng, D. et al. Simultaneous bottom-up interfacial and bulk defect passivation in highly efficient planar perovskite solar cells using nonconjugated small-molecule electrolytes. *Adv. Mater.* **31**, 1903239 (2019).
9. Motti, S. G. et al. Defect activity in lead halide perovskites. *Adv. Mater.* **31**, 1901183 (2019).
10. Yang, G. et al. Interface engineering in planar perovskite solar cells: energy level alignment, perovskite morphology control and high performance achievement. *J. Mater. Chem. A* **5**, 1658–1666 (2017).
11. Kim, M. et al. Methylammonium chloride induces intermediate phase stabilization for efficient perovskite solar cells. *Joule* **3**, 2179–2192 (2019).
12. Yin, W.-J., Shi, T. & Yan, Y. Unusual defect physics in CH₃NH₃PbI₃ perovskite solar cell absorber. *Appl. Phys. Lett.* **104**, 063903 (2014).
13. Stolterfoht, M. et al. The impact of energy alignment and interfacial recombination on the internal and external open-circuit voltage of perovskite solar cells. *Energy Environ. Sci.* **12**, 2778–2788 (2019).
14. Yang, G. et al. Effective carrier-concentration tuning of SnO₂ quantum dot electron-selective layers for high-performance planar perovskite solar cells. *Adv. Mater.* **30**, 1706023 (2018).
15. Saliba, M. et al. Incorporation of rubidium cations into perovskite solar cells improves photovoltaic performance. *Science* **354**, 206–209 (2016).
16. Yadav, P. et al. The role of rubidium in multiple-cation-based high-efficiency perovskite solar cells. *Adv. Mater.* **29**, 1701077 (2017).
17. Albadri, A. et al. Unraveling the impact of rubidium incorporation on the transport-recombination mechanisms in highly efficient perovskite solar cells by small-perturbation techniques. *J. Phys. Chem. C* **121**, 24903–24908 (2017).
18. Shao, S. et al. Highly reproducible Sn-based hybrid perovskite solar cells with 9% efficiency. *Adv. Energy Mater.* **8**, 1702019 (2018).
19. Cao, D. H., Stoumpos, C. C., Farha, O. K., Hupp, J. T. & Kanatzidis, M. G. 2D homologous perovskites as light-absorbing materials for solar cell applications. *J. Am. Chem. Soc.* **137**, 7843–7850 (2015).
20. Lee, J.-W. et al. Formamidinium and cesium hybridization for photo- and moisture-stable perovskite solar cell. *Adv. Energy Mater.* **5**, 1501310 (2015).
21. Zhang, T. et al. Crystallinity preservation and ion migration suppression through dual ion exchange strategy for stable mixed perovskite solar cells. *Adv. Energy Mater.* **7**, 1700118 (2017).
22. Baldan, A. Review progress in Ostwald ripening theories and their applications to nickel-base superalloys. Part I: Ostwald ripening theories. *J. Mater. Sci.* **37**, 2171–2202 (2002).
23. Yang, G., Qin, P., Fang, G. & Li, G. A Lewis base-assisted passivation strategy towards highly efficient and stable perovskite solar cells. *Sol. RRL* **2**, 1800055 (2018).
24. Abdi-Jalebi, M. et al. Maximizing and stabilizing luminescence from halide perovskites with potassium passivation. *Nature* **555**, 497–501 (2018).
25. Wang, Z. et al. Efficient ambient-air-stable solar cells with 2D–3D heterostructured butylammonium-caesium-formamidinium lead halide perovskites. *Nat. Energy* **2**, 17135 (2017).
26. Eperon, G. E. et al. Formamidinium lead trihalide: a broadly tunable perovskite for efficient planar heterojunction solar cells. *Energy Environ. Sci.* **7**, 982–988 (2014).
27. Rau, U. Reciprocity relation between photovoltaic quantum efficiency and electroluminescent emission of solar cells. *Phys. Rev. B* **76**, 085303 (2007).
28. Tress, W. et al. Interpretation and evolution of open-circuit voltage, recombination, ideality factor and subgap defect states during reversible light-soaking and irreversible degradation of perovskite solar cells. *Energy Environ. Sci.* **11**, 151–165 (2018).
29. Green, M. A. Radiative efficiency of state-of-the-art photovoltaic cells. *Prog. Photovolt. Res. Appl.* **20**, 472–476 (2012).
30. Bi, D. et al. Efficient luminescent solar cells based on tailored mixed-cation perovskites. *Sci. Adv.* **2**, e1501170 (2016).
31. Liu, J., Leng, J., Wu, K., Zhang, J. & Jin, S. Observation of internal photoinduced electron and hole separation in hybrid two-dimensional perovskite films. *J. Am. Chem. Soc.* **139**, 1432–1435 (2017).
32. Nelson J. *The Physics of Solar Cells* (World Scientific, 2003).
33. Turren-Cruz, S.-H. et al. Enhanced charge carrier mobility and lifetime suppress hysteresis and improve efficiency in planar perovskite solar cells. *Energy Environ. Sci.* **11**, 78–86 (2018).
34. Lin, Y. et al. Unveiling the operation mechanism of layered perovskite solar cells. *Nat. Commun.* **10**, 1008 (2019).
35. Sarritzu, V. et al. Optical determination of Shockley-Read-Hall and interface recombination currents in hybrid perovskites. *Sci. Rep.* **7**, 44629 (2017).
36. Jackson, W. B., Amer, N. M., Boccara, A. & Fournier, D. Photothermal deflection spectroscopy and detection. *Appl. Opt.* **20**, 1333–1344 (1981).
37. Stranks, S. D. et al. Recombination kinetics in organic-inorganic perovskites: excitons, free charge, and subgap states. *Phys. Rev. Appl.* **2**, 034007 (2014).
38. Stranks, S. D. Nonradiative losses in metal halide perovskites. *ACS Energy Lett.* **2**, 1515–1525 (2017).
39. Shao, Y., Yuan, Y. & Huang, J. Correlation of energy disorder and open-circuit voltage in hybrid perovskite solar cells. *Nat. Energy* **1**, 15001 (2016).

40. Chen, B., Rudd, P. N., Yang, S., Yuan, Y. & Huang, J. Imperfections and their passivation in halide perovskite solar cells. *Chem. Soc. Rev.* **48**, 3842–3867 (2019).
41. McMeekin, D. P. et al. A mixed-cation lead mixed-halide perovskite absorber for tandem solar cells. *Science* **351**, 151–155 (2016).
42. Zhao, D. et al. Four-terminal all-perovskite tandem solar cells achieving power conversion efficiencies exceeding 23%. *ACS Energy Lett.* **3**, 305–306 (2018).
43. Yu, Y. et al. Synergistic effects of lead thiocyanate additive and solvent annealing on the performance of wide-bandgap perovskite solar cells. *ACS Energy Lett.* **2**, 1177–1182 (2017).
44. Zhou, Y. et al. Benzylamine-treated wide-bandgap perovskite with high thermal-photostability and photovoltaic performance. *Adv. Energy Mater.* **7**, 1701048 (2017).
45. Domanski, K., Alharbi, E. A., Hagfeldt, A., Grätzel, M. & Tress, W. Systematic investigation of the impact of operation conditions on the degradation behaviour of perovskite solar cells. *Nat. Energy* **3**, 61–67 (2018).
46. Kong, J. et al. Long-term stable polymer solar cells with significantly reduced burn-in loss. *Nat. Commun.* **5**, 5688 (2014).
47. Chen, B. et al. Synergistic effect of elevated device temperature and excess charge carriers on the rapid light-induced degradation of perovskite solar cells. *Adv. Mater.* **31**, e1902413 (2019).
48. Lin, Y. et al. Excess charge-carrier induced instability of hybrid perovskites. *Nat. Commun.* **9**, 4981 (2018).

Methods

Preparation of RbCsMAFA (Rb$_{0.05}$Cs$_{0.05}$[(FA$_{0.83}$MA$_{0.17}$)]$_{0.9}$Pb(I$_{0.83}$Br$_{0.17}$)$_3$). First, a non-stoichiometric precursor solution for (FA$_{0.83}$MA$_{0.17}$)Pb(I$_{0.83}$Br$_{0.17}$)$_3$ was prepared by dissolving 1.1 M PbI$_2$ (TCI), 1 M FAI (Dyesol), 0.22 M PbBr$_2$ and 0.2 M MABr (Dyesol) in a 4:1 (v/v) mixture (1 ml) of anhydrous dimethylformamide (DMF) and dimethyl sulfoxide (DMSO), respectively. (Please note the volume changes upon dissolving these salts.) Then, 1.5 M CsI (40 µl; Alfa Aesar) pre-dissolved in DMSO (1 ml) and 1.5 M RbI (40 µl; Alfa Aesar) pre-dissolved in a 4:1 (v/v) mixture (1 ml) of anhydrous DMF and DMSO were added to the as-prepared (FA$_{0.83}$MA$_{0.17}$)Pb(I$_{0.83}$Br$_{0.17}$)$_3$ solution, yielding the quadruple-cation perovskite of composition Rb$_{0.05}$Cs$_{0.05}$[(FA$_{0.83}$MA$_{0.17}$)]$_{0.9}$Pb(I$_{0.83}$Br$_{0.17}$)$_3$. The quadruple-cation perovskite solution was stirred for 6 h at room temperature and then filtered using a 0.45 µm filter before use. For RbCsMAFA film deposition, the perovskite precursor solution (50 µl) was spin coated onto the substrates at 1,000 and 5,000 revolutions per minute (r.p.m.) for 10 and 20 s, respectively. Chlorobenzene (105 µl) was added dropwise onto the perovskite film at 25 s from the start of the spinning process. The perovskite films were then placed on a hot plate at 100 °C for 60 min.

Preparation of MA$_{0.7}$FA$_{0.3}$PbI$_3$. The MA$_{0.7}$FA$_{0.3}$PbI$_3$ precursor solution contained 1.25 M PbI$_2$, methylammonium iodide and formamidinium iodide (PbI$_2$:MAI:FAI = 1:0.7:0.3) in a mixed solvent of DMF and DMSO (volume ratio: 4:1). Pb(SCN)$_2$ (12 mg; Sigma-Aldrich) was then added to the MA$_{0.7}$FA$_{0.3}$PbI$_3$ precursor solution (1 ml). For MA$_{0.7}$FA$_{0.3}$PbI$_3$ film deposition, the perovskite precursor solution (50 µl) was spin coated onto the substrates at 1,000 and 4,000 r.p.m. for 5 and 30 s, respectively. Chlorobenzene (300 µl) was added dropwise onto the perovskite film at 13–15 s from the start of the spinning process. Then the as-deposited film was annealed at 65 °C for 2 min and at 100 °C for 10 min.

Preparation of FA$_{0.8}$Cs$_{0.2}$Pb(I$_{0.7}$Br$_{0.3}$)$_3$. The FA$_{0.8}$Cs$_{0.2}$Pb(I$_{0.7}$Br$_{0.3}$)$_3$ precursor solution contained 0.8 M FAI, 0.2 M CsI, 0.55 M PbI$_2$, 0.45 M PbBr$_2$ and 0.55% M Pb(SCN)$_2$ in a mixed solvent of DMF and DMSO (volume ratio: 3:1). For FA$_{0.8}$Cs$_{0.2}$Pb(I$_{0.7}$Br$_{0.3}$)$_3$ film deposition, the perovskite precursor solution (50 µl) was spin coated onto the substrates at 1,000 and 4,000 r.p.m. for 5 and 30 s, respectively. Chlorobenzene (300 µl) was added dropwise onto the perovskite film at 13–15 s from the start of the spinning process. The as-prepared film was then annealed at 65 °C for 2 min and at 100 °C for 10 min.

Preparation of Cs$_{0.03}$(FA$_{0.97}$MA$_{0.03}$)$_{0.97}$Pb(I$_{0.97}$Br$_{0.03}$)$_3$. The Cs$_{0.03}$(FA$_{0.97}$MA$_{0.03}$)$_{0.97}$Pb(I$_{0.97}$Br$_{0.03}$)$_3$ precursor solution was prepared using the mixed powders of FAI:MABr:MACl:PbBr$_2$:PbI$_2$ (molar ratio: 1.41:0.04:0.4:0.04:1.47) in a mixed solvent of DMF and DMSO (volume ratio: 4:1), blended with CsI (1.5 M; 3% volume ratio) stock solution. For Cs$_{0.03}$(FA$_{0.97}$MA$_{0.03}$)$_{0.97}$Pb(I$_{0.97}$Br$_{0.03}$)$_3$ film deposition, the perovskite solution (50 µl) was spin coated onto the SnO$_2$-coated ITO substrate at 1,000 and 6,000 r.p.m. for 10 and 30 s, respectively. Chlorobenzene (150 µl) was added dropwise onto the perovskite film at 15–20 s from the start of the spin-coating process. The as-prepared films were annealed at 120 °C for 1 h under an ambient atmosphere with ~20% RH.

For the dimensionally graded passivation method, BABr–isopropyl alcohol solution (100 µL; the concentrations ranged from 1 to 5 mg ml^{-1}) was spin coated onto the as-prepared perovskite films at 5,000 r.p.m. for 30 s. Then the perovskite films were annealed at 100 °C for 10 min.

Perovskite solar cell fabrication. *Fabrication of n–i–p solar cells.* The ITO-coated glass was sequentially cleaned using deionized water, acetone and ethanol. All substrates were further cleaned via UV-ozone treatment for 15 min before deposition of the SnO$_2$ ETL. The SnO$_2$ QD ETL (30 nm thick) was deposited on the cleaned ITO substrate by spin coating with an as-prepared colloidal SnO$_2$ QD solution[14]. Then the as-deposited SnO$_2$ QD ETL was annealed on a hot plate at 200 °C for 1 h in air. The mixed-cation perovskite was deposited via a one-step spin-coating procedure as mentioned above. The spiro-OMeTAD solution (20 µl), which contained spiro-OMeTAD (72.3 mg; Lumitech), *tert*-butylpyridine (28.8 µl; Sigma-Aldrich), bis(trifluoromethanesulfonyl)imide (17.5 µl; LiTFSI, Sigma-Aldrich) solution (520 mg in acetonitrile) and chlorobenzene (1 ml), was spin coated onto the perovskite layer at 3,000 r.p.m. for 20 s. Finally, an 80-nm-thick layer of gold was deposited by thermal evaporation.

Fabrication of p–i–n solar cells. Poly(triaryl amine) solution (2 mg ml^{-1} in toluene) was spin coated onto the perovskite layer at 5,000 r.p.m. for 30 s and annealed at 100 °C for 10 min. A 1.63 eV perovskite layer was deposited on the poly(triaryl amine) layer using the same method as based on one-step approach. Then, a 30-nm-thick C$_{60}$ layer (the ETL) and a 12-nm-thick SnO$_2$ layer (the buffer layer) were deposited by thermal evaporation and atomic layer deposition, respectively. Finally, a 100-nm-thick layer of copper was deposited as the top metal electrode by thermal evaporation.

Solar cell characterization. The current density–voltage (*J–V*) characteristics of the devices were measured using a Keithley 2400 Source Meter under standard AM1.5 G illumination (SS-F5; Enli Technology, Taiwan), and the light intensity was calibrated using a standard SRC-2020 silicon reference cell. The *J–V* curves were obtained in the range from 1.3 to −0.1 V with a scan speed of 100 mV s^{-1} from both reverse and forward scan directions. The active area of the device is 0.09 cm^2, and a mask with an aperture area of 0.0625 cm^2 was used to define the device area. The stabilized output of the devices was measured by recording the current output of the illuminated device while holding it at a constant voltage near the MPP extracted from the *J–V* curve.

Solar cell certification. Device certification was conducted by the Enli Technology Optoelectronic Calibration Laboratory, a photovoltaic certification laboratory accredited by the Taiwan Accreditation Foundation (accreditation criteria: ISO/IEC 17025:2005).

Photostability test. The devices are kept under an array of white LEDs with 0.8-Sun intensities, which was calibrated using a standard silicon solar cell (KG5). The encapsulated devices were exposed to RH below 20% at ~35 °C.

External quantum efficiency. EQE measurements of the photovoltaic devices were carried out from 300 to 850 nm using a QE-R 3011 system (Enli Technology, Taiwan).

X-ray diffraction and grazing-incidence wide-angle X-ray scattering characterization. The crystal structure and phase of the materials were characterized using an X-ray diffractometer (Rigaku SmartLab) with Cu Kα radiation under operating conditions of 40 kV and 40 mA (with the θ–2θ scan mode from 10 to 70° in steps of 0.01°). The GIWAXS measurements were carried out using a Xeuss 2.0 SAXS/WAXS laboratory beamline with a copper X-ray source (8.05 keV, 1.54 Å) and a Pilatus3 R 300K detector. The angle of incidence is 0.3°. The perovskite films for X-ray diffraction and GIWAXS characterizations were deposited on SnO$_2$-coated ITO substrates.

Scanning electron microscopy. The morphologies and microstructures were investigated by using a TESCAN MAIA3 field emission scanning electron microscope. The perovskite films for SEM measurement were prepared on SnO$_2$-coated ITO substrates.

Atomic force microscopy. A Bruker NanoScope 8 atomic force microscope was used to measure the height and phase profiles of the perovskite films in tapping mode. The perovskite films for AFM measurement were prepared on SnO$_2$-coated ITO substrates.

Photothermal deflection spectroscopy. For PDS measurements, the perovskite film was deposited on a quartz substrate and then immersed into Fluorinert FC-72 (3M). A monochromatic light beam was modulated at 13 Hz by a mechanical chopper to excite the perovskite films from the quartz side. A laser was at the perpendicular side so that it was deflected periodically. A position detector, connected with a lock-in amplifier, was placed on the other side so that the beam deflection signal was measured.

Time-of-flight secondary-ion mass spectroscopy. The perovskite films were deposited on ITO substrates for ToF-SIMS measurement. The ToF-SIMS measurements (Model TOF.SIMS 5, ION-TOF) were conducted using pulsed primary ions from a Cs$^+$ (3 keV) liquid-metal ion gun or C$_{60}$ (10 keV) sputtering and a Bi$^+$ pulsed primary ion beam for the analysis (25 keV).

Time-resolved photoluminescence and photoluminescence spectra. PL measurements of perovskite films on glass substrates were conducted using an FLSP920 spectrophotometer (Edinburgh Instruments) installed with a 485 nm picosecond pulsed diode laser excitation source with an average power of 0.15 mW.

Ultraviolet-visible absorption spectra. The absorption spectra of the perovskite films were measured using a UV-visible spectrophotometer (Cary 5000, Varian) in the 300–850 nm wavelength range at room temperature.

Ultraviolet photoelectron spectroscopy. Samples for UPS measurements were prepared by depositing perovskite films on ITO conductive substrates. The UPS measurements were obtained using an XPS/UPS system (Escalab 250Xi, Thermo Scientific).

Photoluminescence quantum efficiency. The PLQE of the perovskite films was measured using an integrating sphere (Edinburgh instruments) with a 485 nm excitation laser (~125 mW cm^{-2}) in open-air conditions.

External quantum efficiency of the electroluminescence. The EQE$_{EL}$ of the solar cells was determined by measuring the emitted photons of the devices in all directions through an integrated sphere by using a calibrated spectrometer (QE Pro, Ocean Optics), under a constant current density provided by a Keithley 2400 source measure unit. The devices were left at room temperature in open-air conditions.

Trap density of states. Admittance spectra were measured by using an Agilent E4980A meter with an alternating voltage of 20 mV. The frequency dependence of the capacitance was recorded from 1 kHz to 2,000 kHz with zero bias in the dark.

Transmission electron microscope characterization. TEM lift-out samples were prepared via FIB polishing using a TESCAN GAIA3 FIB-SEM instrument. A covering layer of 1.5-μm-thick platinum was deposited by an electron beam. Then the TEM lamella was extracted by the FIB, which had an ion beam accelerating voltage of 30 kV and a current of 7 nA, and welded to a TEM copper grid by platinum. After that, the TEM lamella was polished to about 300 nm thick with an accelerating voltage of 30 kV and a current of 100 pA. Finally, it was thinned to electron transparency with an accelerating voltage of 5 kV and a current of 25 pA and an accelerating voltage of 2 kV and a current of 20 pA. Accelerating voltage for SEM observation and electron-beam deposition was kept at 5 kV during the whole process. The TEM lift-out sample was sent into the TEM chamber less than one minute after sample preparation. TEM observations were carried out using a JEOL ARM200CF transmission electron microscope equipped with a cold field emission electron gun and double spherical-aberration correctors (CEOS) operated at 80 kV.

Density functional theory calculations. All calculations were performed based on the DFT calculations using the Vienna ab initio simulation package code with the standard frozen-core projector augmented-wave method. The generalized gradient approximation of the Perdew–Burke–Ernzerhof functional was employed for the exchange-correlation potential. The cutoff energy for basis functions is 400 eV and the k-point mesh was obtained using the Monkhorst–Pack method with a reasonable grid density. Atoms are fully relaxed until the Hellmann–Feynman forces on them are 0.01 eV Å^{-1} and the vacuum layer is 15 Å, which is long enough to reach the calculation precision. The effect of van der Waals interactions was considered using the empirical correction method proposed by Grimme (DFT-D3) with Becke–Johnson damping. Dipole correction was applied to compensate for the dipole interaction.

Reporting Summary. Further information on research design is available in the Nature Research Reporting Summary linked to this article.

Data availability
The data that support the plots within this paper and other findings of this study are available from the corresponding author upon reasonable request.

Author contributions
G.L., G.Y. and Y.Y. proposed the idea and designed the experiment. G.Y. and Z.R. fabricated and characterized the PSCs. Z.R., K.L., H.Z. and Q.L. prepared and characterized the devices for the PSC efficiency certification. G.Y. conducted SEM, AFM, X-ray diffraction and PL measurements. X.L. and M.Q. carried out GIWAXS measurements and analysed the results. W.D. and H.Wu conducted the EL measurements and discussed the radiative and non-radiative recombination loss analysis. Y.C. performed DFT calculations on the BA molecule passivation under the supervision of T.S. and X.W. Both B.G. and J.H. helped to measure the ultrasensitive EQE. D.L. and S.L. contributed to the PLQY measurements. J.L., H.Wang and F.Y. carried out the UPS and absorption measurements. H.Y. and S.K.S contributed to the PDS data. H.Z. contributed to the analysis of the ToF-SIMS results. Y.Z performed the HRTEM measurements and analysed the results under the supervision of J.W. The manuscript was prepared, revised and finalized by G.L., G.F., Y.Y., G.Y., Z.R., K.L. and X.L. All authors discussed the results and commented on the manuscript.

Competing interests
The authors declare no competing interests.

Additional information
Supplementary information The online version contains supplementary material available at https://doi.org/10.1038/s41566-021-00829-4.

Correspondence and requests for materials should be addressed to Y.Y., G.F. or G.L.

Reprints and permissions information is available at www.nature.com/reprints.

nature research

Corresponding author(s): NPHOT-2018-09-01237A

Solar Cells Reporting Summary

Nature Research wishes to improve the reproducibility of the work that we publish. This form is intended for publication with all accepted papers reporting the characterization of photovoltaic devices and provides structure for consistency and transparency in reporting. Some list items might not apply to an individual manuscript, but all fields must be completed for clarity.

For further information on Nature Research policies, including our data availability policy, see Authors & Referees.

▶ Experimental design

Please check: are the following details reported in the manuscript?

1. Dimensions

   Area of the tested solar cells — ☒ Yes ☐ No — Active area of the tested solar cells is 0.09 cm2 (Methods).

   Method used to determine the device area — ☒ Yes ☐ No — The active area was determined by the crossed area of counter electrode and ITO stripe. A 0.0625 cm2 aperture was used during solar cells testing (certified 0.06195 cm2, Enli Tech. Optoelectronic Calibration Lab., Taiwan).

2. Current-voltage characterization

   Current density-voltage (J-V) plots in both forward and backward direction — ☒ Yes ☐ No — See Figure 3, Supplementary Figure 7, 17, and 23.

   Voltage scan conditions
   For instance: scan direction, speed, dwell times — ☒ Yes ☐ No — J-V curves were measured by forward scan (-0.1 to 1.3 V) and reverse scan (1.3 to -0.1 V) in a scanning rate of 100 mV/s (voltage step: 20 mV, delay time: 100 ms) (Methods).

   Test environment
   For instance: characterization temperature, in air or in glove box — ☒ Yes ☐ No — In glove box at room temperature.

   Protocol for preconditioning of the device before its characterization — ☐ Yes ☒ No — No precondition before testing.

   Stability of the J-V characteristic
   Verified with time evolution of the maximum power point or with the photocurrent at maximum power point; see ref. 7 for details. — ☒ Yes ☐ No — Maximum power point testing was performed (see Figure 3).

3. Hysteresis or any other unusual behaviour

   Description of the unusual behaviour observed during the characterization — ☒ Yes ☐ No — The control devices showed moderate hysteresis in J-V curve, while the DGPF based devices showed hysteresis-free behaviors.

   Related experimental data — ☒ Yes ☐ No — See Figure 3, Supplementary Figure 9, 22, 25 and 27, Supplementary Table 4 and 7.

4. Efficiency

   External quantum efficiency (EQE) or incident photons to current efficiency (IPCE) — ☒ Yes ☐ No — See Figure 3 and Supplementary Figure 4, 9, 20, and 21.

   A comparison between the integrated response under the standard reference spectrum and the response measure under the simulator — ☒ Yes ☐ No — The integrated Jsc from EQE spectrum is agreed well (less than 3% mismatch) with the Jsc from J-V measurement.

   For tandem solar cells, the bias illumination and bias voltage used for each subcell — ☐ Yes ☒ No — No tandem solar cell was reported in this manuscript.

5. Calibration

   Light source and reference cell or sensor used for the characterization — ☒ Yes ☐ No — Enli Technology AAA solar simulator (SS-F5) and standard Si (SRC-2020) reference cell were used during solar cells testing (Methods).

Confirmation that the reference cell was calibrated and certified

☒ Yes No

The reference cell (SRC-2020) was calibrated by NREL.

Calculation of spectral mismatch between the reference cell and the devices under test

 Yes ☒ No

No spectral mismatch calculation was performed in our lab.

6. Mask/aperture

Size of the mask/aperture used during testing

☒ Yes No

A 0.0625 cm2 aperture was used during solar cells testing (certified 0.06195 cm2, Enli Tech. Optoelectronic Calibration Lab., Taiwan).

Variation of the measured short-circuit current density with the mask/aperture area

 Yes ☒ No

We didn't measure the solar cells with apertures of different sizes.

7. Performance certification

Identity of the independent certification laboratory that confirmed the photovoltaic performance

☒ Yes No

Solar cells were certified by Enli Tech. Optoelectronic Calibration Lab., Taiwan.

A copy of any certificate(s)
Provide in Supplementary Information

☒ Yes No

See Supplementary Figure 25.

8. Statistics

Number of solar cells tested

☒ Yes No

20 devices for each condition were tested.

Statistical analysis of the device performance

☒ Yes No

See Supplementary Figure 4.

9. Long-term stability analysis

Type of analysis, bias conditions and environmental conditions
For instance: illumination type, temperature, atmosphere humidity, encapsulation method, preconditioning temperature

☒ Yes No

Long-term stability with 0.8 sun illumination under open-circuit condition (20-30% RH, 35-40 °C) and with 1 sun illumination under MPP tracking (30-40% RH, 60-65 °C) (Figure 4).